Robust Carbon-Nanotube-Based Nano-electromechanical Devices: Understanding and Eliminating Prevalent Failure Modes Using Alternative Electrode Materials

*Owen Loh, Xiaoding Wei, Changhong Ke, John Sullivan, and Horacio D. Espinosa**

The International Technology Roadmap for Semiconductors (ITRS[1]) identifies emerging technologies with the potential to sustain Moore's Law. A necessary succession from planar CMOS (complementary metal-oxide semiconductors) to nonplanar/dual-gate CMOS, and ultimately to novel architectures such as carbon nanotube (CNT)-based nano-electromechanical systems (NEMS) is envisioned. The ITRS also identifies critical roadblocks currently precluding advances beyond CMOS. Primary among the roadblocks to NEMS are poor reliability and manufacturing challenges. Here we investigate the prevalent failure modes of CNT-based NEMS that hamper reliability through a combined experimental–computational approach. We first identify their point of onset within the design space through in situ electromechanical characterization, highlighting the extremely limited region in which failure is avoided. We use dynamic multiphysics models to elucidate the underlying causes of failure, then return to the experimental characterization to show that the usable design space expands dramatically when employing novel electrode materials such as diamondlike carbon. Finally, we demonstrate the efficacy of this solution through 100 successive actuation cycles without failure and applications to volatile memory operations.

The immense potential of CNT-based NEMS is emergent in theoretical and experimental demonstrations of up to 100-GHz switching,[2] low leakage, and high ON–OFF ratios,[3] and outstanding current-carrying capacity.[4,5] To date however, individual demonstrations of performance such as these have been a primary focus, with limited reports of repeated actuation beyond a few cycles.[2,3,6,7] This is due in large part to critical challenges in device reliability. As a consequence of their ultrahigh performance, these devices experience extreme (and coupled) mechanical, electrical, and thermal loads during normal operation. Furthermore, previously insignificant van der Waals interactions and adhesive forces begin to dominate at this scale. These factors combine to create a number of failure modes that are prevalent among reported devices. Thus finding a solution to suppress or eliminate the onset of failure is critical to the widespread integration of CNT-based NEMS and will represent a significant milestone along the ITRS path.

In this work, an electrostatically actuated CNT switch[8–10] serves as a platform to study prevalent failure modes in CNT-based NEMS. This switch is chosen because it shares operating principles (and thus failure modes) with many reported devices, making the findings of this study broadly applicable. The device consists of a multiwalled CNT of length L that is fixed at one end and cantilevered a distance H above an electrode (**Figure 1**a). The electrical circuit is completed by a voltage source, V, and an external resistor, R_f. When the applied bias exceeds a critical "pull-in voltage" ($V > V_{PI}$), the CNT accelerates toward the electrode, closing the switch. Subsequent reduction of the applied bias results in re-opening of the switch.[8] The electrical domain can be represented by an equivalent lumped-element circuit (Figure 1b) comprising the voltage source and external resistor in series with, in parallel, the parasitic capacitance of the system, C_0, the capacitance of the CNT cantilever relative to the electrode, C_{CNT}, and the lumped CNT and tunneling/contact resistance, R_{CNT}, when the CNT approaches and makes contact with the electrode. Note that C_{CNT} and R_{CNT} will depend upon the CNT–electrode gap (see Experimental Section and Section 1 of Supporting Information). The total current is denoted as I_{total}, while the current through the CNT is I_{CNT}. U is the potential across the CNT, where $U = V$ when $I_{total} = 0$.

A parametric study was first conducted to identify prevalent failure modes and their point of onset within the device design space. The design space investigated comprises the CNT length L and CNT–electrode gap H, which are perhaps the two most readily controlled parameters when using common micro/nanofabrication techniques to produce freestanding nanostructures.[3,11–13] While devices of larger dimensions were also tested, experiments were focused in the $0 < L < 2$ μm and $0 < H < 1$ μm range as there is a continuous push for smaller devices.

O. Loh, Dr. X. Wei, Prof. H. D. Espinosa
Dept. of Mechanical Engineering
Northwestern University
2145 Sheridan Rd., Evanston, IL 60208–3111, USA
E-mail: espinosa@northwestern.edu
Prof. C. Ke
Dept. of Mechanical Engineering
State University of New York and Binghamton
PO Box 6000, Binghamton, NY 13902, USA
Dr. J. Sullivan
Center for Integrated Nanotechnologies
Sandia National Laboratories
MS1304, PO Box 5800, Albuquerque, NM 87185, USA

DOI: 10.1002/smll.201001166

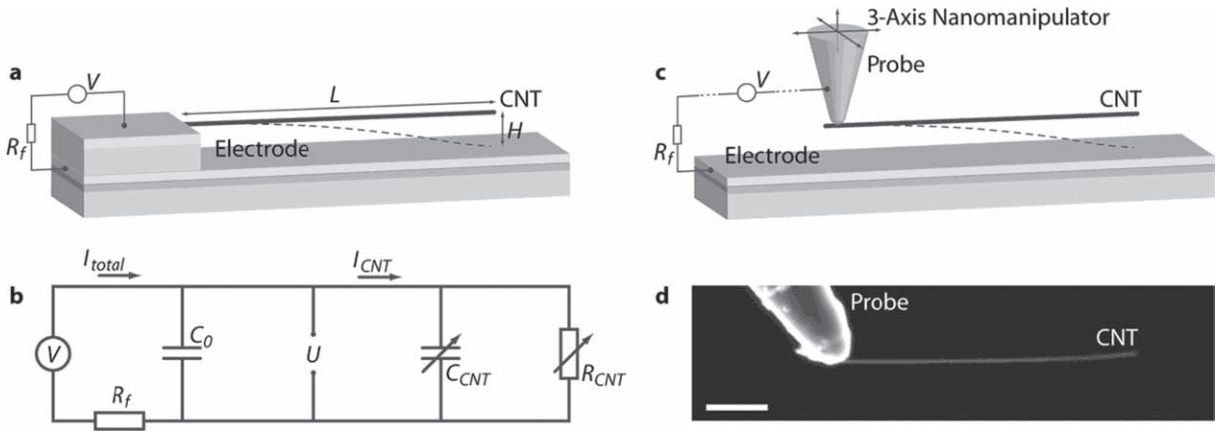

Figure 1. Overview of cantilevered CNT switch used as a platform to study failure modes. a) Schematic of switch consisting of a CNT cantilevered over a metal thin-film electrode. b) Equivalent lumped-element circuit for the device. c) Nanomanipulaton-based experimental set-up used to recreate the device geometry shown in (a), enabling real-time incremental variation of device geometry and simultaneous electromechanical characterization in situ the scanning electron microscope. The voltage source *V* is the only component exterior to the scanning electron microscope chamber. d) Scanning electron micrograph showing a CNT mounted on the tip of a nanomanipulator probe approaching the electrode. Scale bar is 1 μm.

To test a large number of device geometries spanning the design space in a more statistically significant study, an in situ nanomanipulation-based technique was adopted over conventional microfabrication processes to construct the devices. A three-axis nanomanipulator was used to position cantilevered CNTs over an electrode (Figure 1c,d; also see Experimental Section), effectively recreating the platform device (Figure 1a). This allowed real-time prescription of device geometry with simultaneous voltage application (V), measurement of total current (I_{total}), and imaging of device operation and failure via scanning electron microscopy (SEM). For example, a device of a given L could be repeatedly characterized with incrementally decreasing H by using the manipulator to progressively step the CNT closer to the electrode. In this initial parametric study, a gold-coated substrate was used as an electrode as reported devices ubiquitously use metal thin-film electrodes.[3,8,11,14,15]

Two common modes of failure were observed (**Figure 2**). For relatively long cantilevers and small CNT–electrode gaps, irreversible stiction preventing re-opening of the switch was observed (Figure 2a–c,f). The corresponding I_{total}–V response (Figure 2a) shows a well-defined jump in current upon pull-in, followed by a linear decrease to zero as the applied voltage is ramped back down. This linear behavior is characteristic of maintained Ohmic contact between the CNT and electrode. Imaging the device following actuation confirmed that the CNT indeed remained stuck to the electrode after the applied bias was fully released (Figure 2c). This irreversible stiction has been widely reported and is known to be the result of strong van der Waals interactions between the CNT and electrode.[2,6,12,14,16] When these adhesive interactions exceed the elastic restoring force in the deformed cantilever, the switch does not re-open, even when the bias is fully removed. In fact, nanotube–substrate interactions have been shown in some cases to be sufficiently strong to radially collapse the CNT.[17,18] In cases where the device is operated in atmosphere, liquid adhesion adds additional adhesive energy to be overcome.

For relatively short cantilevers with larger CNT–electrode gaps, incremental shortening of the CNT cantilever was observed with successive actuation cycles (Figure 2d–f). Here the characteristic I_{total}–V curve exhibits a sharp drop in current (inset of Figure 2d) as the voltage is ramped down after pull-in, signifying successful re-opening of the switch. However, inspection of the CNT after successive actuation cycles revealed an incremental loss of length (Figure 2e). Similar incremental losses have been reported, as well as more extreme cases of complete loss of the CNT.[8,19–21] Two possible causes are envisioned. During the highly dynamic pull-in event, the CNT experiences large mechanical stresses as it impacts the electrode at high velocity, which could fracture the CNT. Alternatively, Joule heating resulting from large currents could ablate the nanostructure, resulting in similar loss of length.[19–24]

To further investigate the underlying cause for the observed incremental loss and test potential solutions, a dynamic multiphysics finite element model of the device was developed and implemented in ABAQUS/Explicit.[25] This model treats the mechanical and electrical response of the device through coupled differential equations (i.e., the mechanics of the CNT deformation in response to electrostatic forces, as well as consideration for van der Waals interactions and current flows). It thus enables detailed analysis of the time history of the mechanical stresses and electrical current in the CNT, as well as providing predictive capabilities for CNT-based device design.

The dynamic response of the CNT is described as[26,27]

$$\rho A\frac{\partial^2 r}{\partial t^2} + c\frac{\partial r}{\partial t} + EI\frac{\partial^4 r}{\partial x^4} = q_{elec} + q_{vdW}, \quad (1)$$

where x is the position along the CNT; $r(x,t)$ is the gap between the CNT and electrode; ρ and A are the density and cross-sectional area of the CNT, respectively; c is the damping constant of the system; E is the elastic modulus; I is the moment of inertia and q_{elec} and q_{vdW} represent the load

small NANO MICRO

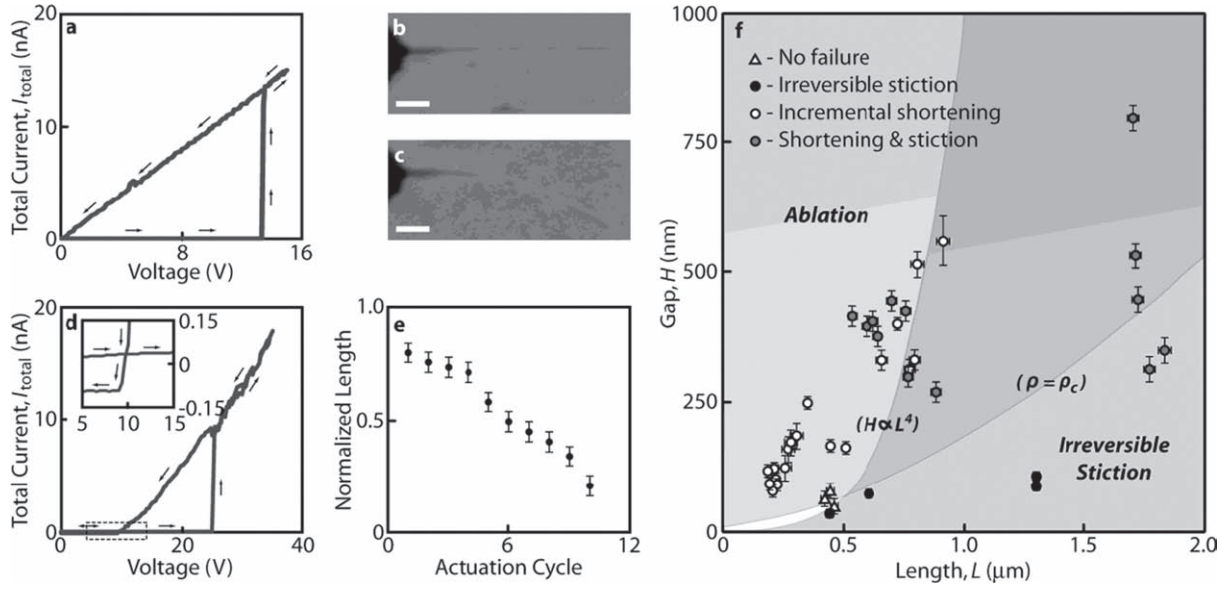

Figure 2. Characteristic failure modes for devices with gold electrodes. a–c) Failure by irreversible CNT–electrode stiction. a) Characteristic measured I_{total}–V response for a device exhibiting irreversible stiction upon pull-in. b,c) Scanning electron micrographs showing the CNT cantilever before and after the actuation cycle respectively. In (c), the CNT clearly remains stuck to the electrode after removing the applied bias. Scale bars are 250 nm. d,e) Failure by incremental loss of CNT length. d) Characteristic measured I_{total}–V response for a device that does not suffer from irreversible stiction. Inset shows detail of the initial upward voltage sweep before pull-in during which the current is slightly positive due to charging of the capacitances, C_0 and C_{CNT}, as well as the pull-out event, after which the current is slightly negative due to gradual discharging of the capacitances as the applied voltage continues to decrease. e) Length of CNT cantilever after successive actuation cycles exhibiting incremental loss. Length is normalized by the initial length before the first cycle. Error bars are defined by the resolution of the SEM images from which the length was measured. f) Map of device geometries tested in the L–H design space and the corresponding failure modes observed. Error bars are again defined by the resolution of the SEM images from which the dimensions were measured. Lines indicate predicted boundaries between failure modes (see Section 2 of Supporting Information). Below a critical elastic restoring force ($H \propto L^4$), irreversible stiction is expected as adhesive forces dominate. Above a critical current density ($\rho = \rho_c$), CNT ablation is expected upon pull-in due to Joule heating.

per unit length on the CNT due to electrostatic and van der Waals interactions with the electrode, respectively (see Section 1 of Supporting Information for full description of these terms and their implementation). The sum of the attractive van der Waals force and electrostatic force on the CNT are treated as a body force (i.e., applied uniformly throughout the volume of the CNT). The repulsive van der Waals force is used to simulate the contact between the CNT and electrode. Both are implemented through user-defined subroutines.

In the simulation, a step input is given at the voltage source, causing the CNT to pull in. Since the resulting bias charge on the CNT is time-dependent, it is necessary to consider the equivalent lumped circuit (Figure 1b) to obtain the charge on the CNT in real time. The equivalent circuit yields

$$R_f\,(C_0 + C_{CNT})\,\frac{dU}{dt} + \left(R_f\frac{dC_{CNT}}{dt} + \frac{R_f}{R_{CNT}} + 1\right)U = V, \quad (2)$$

where C_{CNT} and R_{CNT} depend upon the CNT–electrode gap (see Section 1 of Supporting Information). In the subroutine, the bias on the CNT, U, is updated at each time step by solving Equation 2 numerically.

As the CNT strikes the electrode (**Figure 3**a), a stress wave propagates from the point of contact toward the constrained

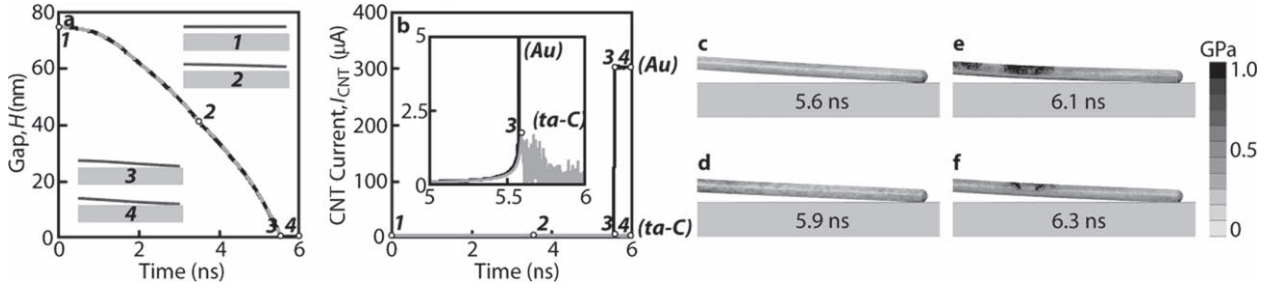

Figure 3. Results of dynamic multiphysics finite-element simulation investigating the cause of incremental CNT loss. a) CNT tip–electrode gap versus time in response to a voltage step applied at time, $t = 0$. The response is shown for devices with gold (solid black line) and ta-C (dashed gray line) electrodes. Insets show snapshots of deformed CNT profile as it deflects toward the electrode. b) Current through CNT (I_{CNT}, see Figure 1b) versus time for devices with gold (black line) and ta-C (gray line) electrodes. Numbered points along the curves correspond in time to those in (a). c–f) Snapshots of stress in tip of the CNT during CNT–electrode impact.

end, and reflects back (Figure 3c–f, see movie in Supporting Information). Additionally, minor buckling is observed momentarily along the CNT (Figure 3e). Although significant, the peak stress observed is approximately one order of magnitude less than the reported failure stress for CNTs obtained from the same source.[28] Thus mechanical fracture alone is an unlikely cause of the observed incremental shortening with repeated actuation (Figure 2e).

Instead of catastrophic mechanical stresses, the dynamic multiphysics analysis reveals a transient spike in current through the CNT (Figure 3b) as it strikes the electrode. This spike, which approaches the milliamp range, is the result of rapid charge dissipation from the capacitances, C_0 and C_{CNT} (Figure 1b), to the substrate. The corresponding current density (see Section 2 of Supporting Information) is more than sufficient to ablate the CNT.[4] In fact, similar observations of incremental loss have been reported in CNT field emitters operated at similar current densities.[19–21] Plotting a line of constant current density in the *L*–*H* design space equivalent to the critical current density required to burn a multiwalled CNT with 25 shells (Figure 2f, see Section 2 of Supporting Information) separates well the experimentally tested cases in which incremental loss was and was not observed, reaffirming the predictions of the model. Here the resulting discharge current density is proportional to the required pull-in voltage (Equation 14 and 15 in Supporting Information). Thus in general, this ablation mechanism becomes more prevalent in shorter-length, larger-gap devices due to the larger required pull-in voltage.

During the initial discharge, $I_{CNT} >> I_{total}$ (Figure 3b). Once the stored charges have been fully depleted and the switch is fully closed, the system reaches a significantly lower steady-state current flow ($I_{total} = I_{CNT} = V/(R_{CNT} + R_f)$, see Figure 1b). Due to the computational cost of the dynamic model, it was not possible to simulate a sufficiently long time period to reach this steady state. However, this steady-state current has been previously predicted analytically for similar devices,[8] and is measured in the present experiments (I_{total}, Figure 2a,d and **Figure 4**a). Here it is important to note that, based upon the equivalent lumped-element circuit (Figure 1b), the spike in I_{CNT} is not expected to appear in the measured I_{total}–V response (Figure 2d). Because the spike arises due to discharge of the capacitances, it remains within the $R_{CNT}C_0$ loop and does not contribute directly to the measured I_{total}. It is also interesting to note that while the mechanical stresses are relatively low and the electrical discharge is alone sufficient to cause failure, the fact that the CNTs are mechanically stressed at the time of the discharge may exacerbate failure. The electrical resistance of CNTs is known to be affected by strain of the lattice structure.[29] This increase in resistance at points of large strain may result in localized regions of elevated Joule heating.

Looking at the highly limited remaining region of the design space in which no failure is predicted (white region in Figure 2f), it is not surprising to find such limited reports of robust, repeated cycling of electrostatically actuated CNT-based NEMS. Perhaps the simplest way to avoid ablation would be to reduce the CNT–electrode gap to decrease the

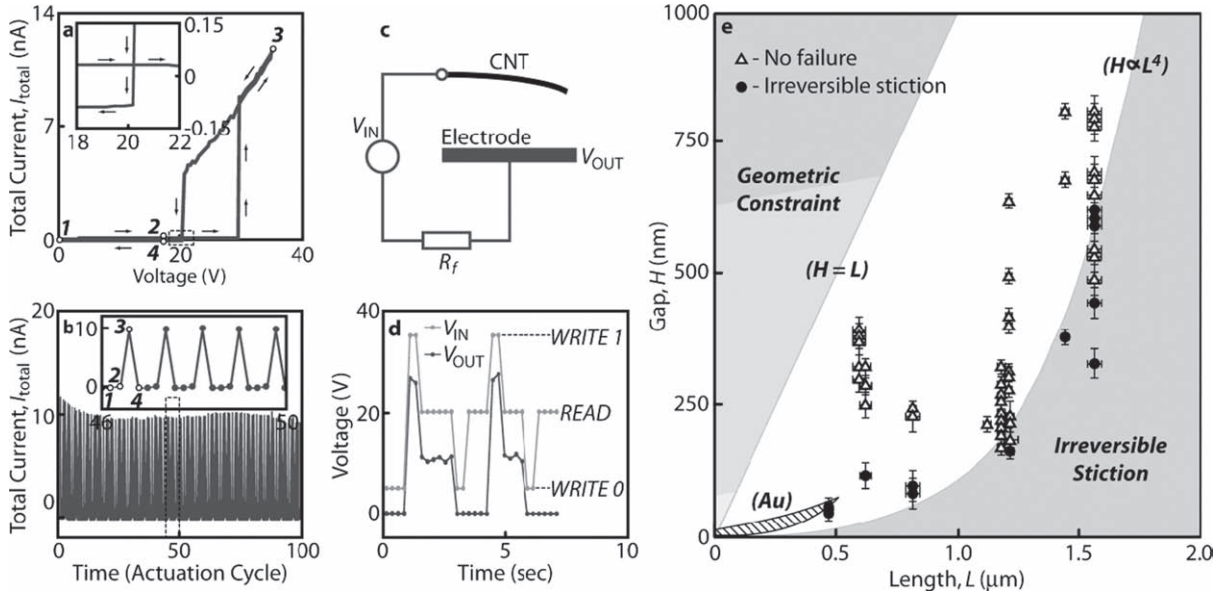

Figure 4. Suppressed failure modes and demonstrated device functionality using diamondlike carbon electrodes. a) Characteristic I_{total}–V curve showing well-defined ON–OFF behavior with significantly less stiction than devices with gold electrodes. Inset shows detail of the initial upward voltage sweep before pull-in, as well as the pull-out event. b) Current profile for 100 successive actuation cycles driven by a 0–35 V triangle wave at the voltage source. Inset shows a detail of cycles 46–50. The numbered data points correspond to the numbered positions in the I_{total}–V curve in (a). c,d) Demonstration of basic volatile memory operation. c) Schematic of voltage input (V_{IN}) used to write '0' or '1' and ouput (V_{OUT}). d) Voltage input and measured output for a series of read and write operations. e) Map of devices tested in the *L*–*H* geometric design space with tetrahedral amorphous carbon, ta-C, electrodes. Error bars are defined by the resolution of the SEM images from which the length and gap dimensions were measured. Incremental shortening/ablation is eliminated, while the onset of stiction is greatly suppressed as compared to those with gold electrodes. For comparison, the dashed area represents the failure-free region determined for devices using gold electrodes (Figure 2f).

required pull-in voltage (and thus the stored charge). However, this promotes stiction. Using CNTs of smaller diameter yields similar results. To avoid this, other devices have employed more complex three-terminal electrode configurations in which a gate electrode at high bias is used to push or pull the CNT into contact with a drain electrode at relatively low bias.[11,14,30–32] In this way the CNT makes contact only with the drain electrode that is at a relatively small potential difference. However, this requires more complex accessing/multiplexing schemes to scale up and may reduce the potential integration density. As such, reports of devices operating without failure or degradation through numerous cycles remain elusive with these architectures.

Examining the equivalent circuit more closely (Figure 1b), increasing R_{CNT} would moderate the detrimental current spike by increasing the time constant for the charge dissipation. However, the contact resistance between CNTs and gold or other conventional metallic electrodes is generally low (measured to be in the kilo-ohms range in our experiments), resulting in rapid discharge and a large current spike at contact.[22] Unfortunately, simply increasing the external resistor R_f would not have a similar effect as it is outside the $R_{CNT}C_0$ loop and thus does not affect the time constant of the discharge.

Diamondlike carbon (tetrahedral amorphous carbon, ta-C) was next considered as an alternative electrode material. Here the contact resistance between the CNT and electrode was measured to be 0.6 GΩ (see Experimental Section), five orders of magnitude greater than for gold. Based upon the previous analysis, this should slow the charge dissipation upon pull-in, thus mitigating the current spike. Before implementing experimentally, this hypothesis was tested using the dynamic multiphysics finite element model. A device of the same geometry and parasitic capacitance was re-simulated with an increased value of contact resistance (R_C = 0.6 GΩ). The resulting mechanics of the switch closing are nearly identical, resulting in similar mechanical stresses. Figure 3a shows the CNT tip–electrode gap as a function of time in which the cases using gold and ta-C electrodes follow nearly identical paths. By contrast, the spike in current through the CNT drops dramatically as expected in the case of the ta-C electrode. Figure 3b compares the current profile through the CNT using the gold and ta-C electrodes. Here we see that the magnitude of the current spike is less than 2.5 μA (as compared to >300 μA for gold), dropping the resulting current density well below the critical value for burning. As the CNT accelerates toward the electrode (point #3 in Figure 3a,b), a small spike in I_{CNT} is still observed due to the rapidly increasing capacitance with decreasing gap before contact, which results in charges being pumped into the CNT. However, because of the increased time constant for capacitance discharge, the stored charge is dissipated over a significantly longer time, resulting in a peak I_{CNT} current closer to the steady-state measured current.

Given these positive predictions, devices with ta-C electrodes were then tested using the same in situ experimental technique. The characteristic I_{total}–V curves exhibited clean pull-in response and well-defined pull-out (Figure 4a) as compared to the gold electrodes (Figure 2a). The observation of sharper pull-out occurring earlier relative to the pull-in voltage suggests decreased CNT–electrode adhesion. This is reflected in the map of failure modes (Figure 4c) where we see greatly suppressed onset of irreversible stiction along the L axis for a given H. This can be attributed to the relatively low surface energy and large contact angle of ta-C as compared to metals such as gold.[33–35]

Perhaps more important though is the complete elimination of any observed incremental loss of CNT length during repeated actuation when using ta-C electrodes (Figure 4e). Even in devices in which the CNT–electrode gap approached the total length of the CNT, no shortening was observed. This elimination of observed shortening supports the model's prediction of significant reduction of the current spike. Rather than being bound by charge dissipation, the design space is now limited by a less severe geometric constraint in which the CNT–electrode gap (H) simply cannot exceed the length (L) of the CNT.

To highlight the efficacy of this solution, a single device was tested through 100 successive actuation cycles by applying a triangle wave at the input voltage. Imaging the device before and after the 100 cycles showed no observable loss of length. Throughout the series of actuation cycles, the measured current versus time (Figure 4b) profile corresponds well to the current versus voltage measured before the cycles (Figure 4a). Given that the predicted mechanical stresses for the ta-C-based devices are similar to those of the Au-based devices, this successful high-cycle demonstration supports the hypothesis that mechanical stresses are not the cause of incremental CNT loss when Au electrodes are employed. It further supports the premise that charge dissipation-induced Joule heating is instead the key mechanism and demonstrates the efficacy of increasing CNT–electrode contact resistance in eliminating this failure mode.

To further demonstrate the functionality of the devices given their improved robustness, basic memory operation was tested. Treating the voltage source (Figure 1b and Figure 4c) as the input and the potential of the electrode as the output (Figure 4c) allows volatile storage of '0' and '1' states. Here the potential of the electrode is pulled high when the CNT makes contact at pull-in, and falls low with pull-out. Figure 4d shows a train of inputs and the corresponding measured output. To write '0', $V_{IN} < V_{PULL\text{-}OUT}$ causes the switch to open and V_{OUT} to go low. To write '1', $V_{IN} > V_{PULL\text{-}IN}$ causes the switch to close and V_{OUT} to go high. To read or store, $V_{PULL\text{-}OUT} < V_{IN} < V_{PULL\text{-}IN}$ holds the switch in its current state.

In summary, the limited reports of successful repeated actuation of CNT-based NEMS using conventional metal electrodes are not surprising given the prevalence of irreversible stiction and ablation failure modes throughout the design space as identified experimentally herein. A dynamic multiphysics model of the device revealed that, in addition to the well-understood irreversible stiction, another dominant failure mode occurs due to Joule-heating-induced ablation. This is the result of rapid dissipation of stored charges upon closing of the CNT switch. Together, these failure modes drastically confine the useful region of the geometric design space. We then showed that the robust, failure-free region of the design space was dramatically expanded through the use

of alternative electrode materials such as ta-C. Using these diamondlike carbon electrodes, we saw not only reduced stiction, but complete elimination of the ablation failure mode. This enabled an unprecedented number of actuation cycles and reliable function as volatile memory, providing motivation for further implementation of alternative materials in improving the performance, robustness, and reliability of electrostatically actuated CNT-based NEMS.

Experimental Section

In situ Device Characterization: In situ electromechanical device characterization was conducted in a Nova NanoSEM (FEI) scanning electron microscope for simultaneous high-resolution imaging and current–voltage measurements. Arc-discharge-grown multiwalled CNTs (n-Tec, Norway) were first dispersed in dry powder form on a copper transmission electron microscopy (TEM) grid (Structure Probe, Inc). The grid was mounted on a Teflon block and placed in the SEM. SEM imaging was used to identify protruding CNTs of the desired length and diameter for device characterization (for all experiments, CNTs of consistent radius (21 ± 3 nm) were selected to allow direct comparison of results between devices of varying length and gap). A three-axis piezoelectric nanomanipulator (Klocke Nanotechnik, Germany) mounted inside the SEM was then used to bring a sharpened tungsten probe (Micromanipulator Co., USA) into contact with the free end of the selected CNT. Electron-beam-induced deposition of carbon was used to fix the CNT in place on the tip of the probe. This deposition technique has been shown to produce near-ideal Ohmic contacts to CNTs.[36] The nanomanipulator was then used to extract the cantilevered CNT and bring it into close proximity to the electrode (also mounted on the same Teflon block to electrically isolate it from the SEM stage). This effectively recreated the platform device geometry (Figure 1a) with the CNT–electrode gap being precisely controlled by the position of the nanomanipulator probe relative to the electrode (Figure 1c).

The probe and electrode were electrically addressable via a feedthrough in the SEM chamber wall. The circuit was completed by insertion of a 1 GΩ resistor (Ohmite Mini-Mox, 992 MΩ actual measured resistance) in line between the electrode and SEM chamber feedthrough. An electrical bias was applied and current simultaneously measured using a parameter analyzer (Keithley 4200-SCS Semiconductor Characterization System). During I_{total}–V measurements, the electron beam of the SEM was blanked as it typically generated noise in the measurements as high as 0.5 nA.

The CNTs were imaged before and after actuation to inspect for failure. CNT length and diameter, and CNT–electrode gap were measured from SEM images using ImageJ software (NIH). The CNT diameter was taken from the full width at half maximum of the intensity profile across the cross section of the CNT in the image.

Electrode Fabrication: Gold electrodes were fabricated by depositing a 100-nm film of gold (with a 10 nm chromium adhesion layer) on a 200-nm-thick silicon nitride-coated silicon wafer by thermal evaporation. A 1-cm^2 piece was then cleaved from the wafer and fixed to the Teflon block as described above. Ta-C electrodes were fabricated by depositing a 140-nm film of ta-C on similar silicon-nitride-coated silicon wafer. To define the proper total electrode resistance and eliminate the need for the external 1 GΩ resistor, long thin traces of ta-C were patterned in the ta-C film. First, a 70-nm aluminum film (with a 10-nm titanium adhesion layer) was deposited by evaporation over the ta-C and patterned by photolithography and liftoff. This was used as an etch mask to define the ta-C electrode shape. The exposed ta-C was etched through to the silicon nitride by reactive ion etching (RIE) using CF_4/O_2. The aluminum etch mask was then stripped by RIE using BCl_3/Cl_2/He to re-expose the ta-C electrodes. Finally the ta-C sample was mounted on a Teflon block in place of the gold electrode.

Measuring Parameters for Multiphysics Model: The multiphysics models require knowledge of the parasitic capacitance and CNT–electrode contact resistances. These were measured experimentally to improve the quantitative accuracy of the models. To measure the parasitic capacitance, the nanomanipulator was first used to bring a CNT into close proximity with the electrode as before. The Keithley 4200-SCS system was then used to source a constant current of 30 fA while measuring the corresponding rise in voltage required to source this current. Assuming the parasitic capacitance is significantly larger than the CNT–electrode capacitance ($C_0 >> C_{CNT}$, where C_{CNT} is on the order of 10^{-17} F[10]), the parasitic capacitance was estimated based upon the time required to ramp from 0 to 1 V at constant current ($C_0 \approx i \cdot \Delta t/\Delta V$). This yielded a parasitic capacitance of about 50 pF for both the Au and ta-C electrode systems.

The measured parasitic capacitance was validated by comparison to the capacitance predicted based upon the magnitude of the slightly positive current observed before pull-in and slightly negative current after pull-out (insets of Figure 2d and Figure 4a). As the voltage is ramped up before pull-in, the only current expected would be due to charging of the parasitic capacitance C_0 (and the relatively small C_{CNT}). Given a fixed value of capacitance, this current is proportional to the rate at which the voltage is swept ($i \approx C_0 \cdot \Delta V/\Delta t$). In these experiments, the voltage was ramped up at a rate of 0.8 V s^{-1}. Given a capacitance of 50 pF, this would yield a current of 0.04 nA as the voltage is ramped up before pull-in. This compares favorably to the experimentally measured currents of 0.03 nA before pull-in. Similarly, after pull-out, the switch is open again at which point the only current expected would be due to discharging of the parasitic capacitance in response to the continued decrease in applied voltage as it is swept back down to zero. In these experiments, the voltage was ramped down at a rate of –2.2 V s^{-1} which, again assuming a capacitance of 50 pF, would yield a current of –0.11 nA as the voltage is ramped down. This compares favorably to the experimentally measured currents of approximately –0.1 nA after pull-out.

The combined CNT/contact resistance R_C (i.e., the resistance of the CNT itself and that of the contact between the CNT and electrode) was estimated first by taking the slope of the I_{total}–V curve after pull-in to calculate the total circuit resistance. From this, the total circuit resistance when the tungsten probe was pressed into direct contact with the electrode (no CNT present) was subtracted. This leaves a combination of the CNT–electrode contact resistance and the resistance of the CNT itself. This calculation is based upon the assumption that the probe–electrode contact resistance is significantly less (because the area of contact is orders of magnitude greater) than the combined CNT and CNT–electrode contact resistance. This yielded a resistance of R_C = 5–50 kΩ for gold, and R_C = 0.6 GΩ for ta-C. Note that in the equivalent lumped element circuit

small NANO MICRO

(Figure 1b), the combined tunneling/contact/CNT resistance term ($R_{CNT} = R_C \exp(\lambda\delta)$, where δ is the gap between the CNT tip and substrate) approaches R_C as $\delta \rightarrow 0$ (see Section 1 of Supporting Information for full details).

We hypothesize that the significantly higher contact resistance in the case of the ta-C may be due in part to the largely differing work functions of CNTs[37] and ta-C[38] (as compared to the closely matched work functions of CNTs and gold[39]), and the high chemical inertness and low adhesion energy of the ta-C. Ohmic contacts of low resistance to diamond materials have generally been achieved only using metals that react to form a carbide at the interface (which one would not expect in the case of CNT–ta-C contact), or by intentionally damaging the diamond surface prior to depositing the contacts.[40] In addition, our parametric studies using gold and ta-C electrodes suggest greater adhesive energy between the CNT and gold electrodes as compared to the ta-C. This greater adhesion between the CNT and gold is likely to facilitate a greater area of contact[17,18] and, in turn, a lower electrical contact resistance.

Multiphysics Finite Element Model: To investigate the dynamic electromechanical response of the device during pull-in, a finite element model was created using ABAQUS/Explicit. In the model, the sum of the attractive van der Waals force and electrostatic force on the carbon nanotube (CNT) were treated as a body force and implemented through the VLOAD subroutine. The repulsive van der Waals force was used to simulate the interaction between the CNT and the substrate and implemented through the VUINTER subroutine. See Section 1 of Supporting Information for full development of this implementation.

In all reported simulations, the following conditions were used. The CNT cantilever had a length of 1.5 μm, an outer radius of 25 nm, and a wall thickness equivalent to a multiwalled CNT having 25 shells assuming an 0.34-nm intershell spacing. The gap between the centerline of the CNT and the electrode was 100 nm. A voltage of 15 V was applied in a step function at $t = 0$ s to actuate the device.

For cases with a gold electrode, the electrode was modeled as an elastic/plastic material with a Young's modulus of 78 GPa, a Poisson's ratio of 0.44, and a yield stress of 10 MPa. For cases with a ta-C electrode, the electrode was modeled as a purely elastic material with a Young's modulus of 87 GPa and a Poisson's ratio of 0.22. For both cases, a value of $R_f = 1$ GΩ was used which, in the case of the gold electrode is representative of the external resistor placed in the circuit (experimentally measured to be 992 MΩ), and for ta-C is representative of the resistance of the ta-C electrode/trace themselves. Experimentally measured values of parasitic capacitance and contact resistance (R_C, see above) were used for both cases.

Estimating Boundaries Between Failure Modes: To test the hypotheses for the causes of failure (as predicted by the finite element model) against the experimental observations, boundaries between the onset of the various failure modes were derived analytically based upon the hypotheses and then plotted over the experimental results in the *L–H* design space (Figure 2f and Figure 4e). For irreversible stiction, this boundary was derived based upon the assumption that the elastic restoring force must exceed the van der Waals adhesive forces. For ablation, this was derived based upon the assumption that burning occurs above a critical current density. These curves of critical elastic restoring force and critical current density were plotted over the experimentally observed cases in the *L–H* design space (see Figure 2f and Figure 4e). Full development of these derivations is provided in Section 2 of Supporting Information.

Supporting Information

Supporting Information is available from the Wiley Online Library or from the author.

Acknowledgements

HDE gratefully acknowledges support from the Army Research Office through award No. W911NF-08–1-0061, and the National Science Foundation through award No. CMMI-0555734. This work was performed in part at the Center for Integrated Nanotechnologies, a U.S. Department of Energy, Office of Basic Energy Sciences user facility at Los Alamos National laboratory (Contract DE-AC52–06NA25396) and Sandia National Laboratories (Contract DE-AC04—94AL85000), and in part at the Center for Nanoscale Materials which is supported by the U.S. Department of Energy, Office of Basic Energy Sciences under Contract No. DE-AC02–06CH11357. The authors gratefully acknowledge assistance from Tobin Filleter regarding nanomanipulation techniques and John Nogan in microfabrication of diamond-like carbon electrodes.

[1] International Roadmap Committee, The international technology roadmap for semiconductors, 2009.
[2] T. Rueckes, K. Kim, E. Joslevich, G. Y. Tseng, C. Cheung, C. M. Lieber, *Science* **2000**, *289*, 94–97.
[3] S. Cha, J. Jang, Y. Choi, G. Amaratunga, D. J. Kang, D. Hasko, J. Jung, J. Kim, *Appl. Phys. Lett.* **2005**, *86*, 083105.
[4] P. Collins, M. Arnold, P. Avouris, *Science* **2001**, *292*, 706–709.
[5] R. Murali, Y. Yang, K. Brenner, T. Beck, J. Meindl, *Appl. Phys. Lett.* **2009**, *94*, 243114.
[6] Y. Hayamizu, T. Yamada, K. Mizuno, R. Davis, D. Futaba, M. Yumura, K. Hata, *Nat. Nanotechnol.* **2008**, *3*, 289–294.
[7] R. Smith, T. Rueckes, S. Konsek, J. Ward, D. Brock, B. Segal, *IEEE Aerospace* **2007**, 1–5.
[8] C. H. Ke, H. D. Espinosa, *Small* **2006**, *2*, 1484–1489.
[9] C. H. Ke, H. D. Espinosa, *J. Appl. Mech.* **2005**, *72*, 721–725.
[10] C. H. Ke, H. D. Espinosa, N. Pugno, *J. Appl. Mech.* **2005**, *72*, 726–731.
[11] Q. Li, S.-M. Koo, M. Edelstein, J. Suehle, C. Richter, *Nanotechnology* **2007**, *18*, 315202.
[12] M. Marcus, J. Simmons, S. Baker, R. Hamers, M. Eriksson, *Nano Lett.* **2009**, *9*, 1806–1811.
[13] S. Lee, D. Lee, H. Yu, E. Campbell, Y. Park, *Appl. Phys. A* **2004**, *78*, 283–286.
[14] S. Lee, D. Lee, R. Morjan, S. Jhang, M. Sveningsson, O. Nerushev, Y. Park, E. Campbell, *Nano Lett.* **2004**, *4*, 2027–2030.
[15] M. Li, R. Bhiladvala, T. Morrow, J. Sioss, K.-K. Lew, J. Redwing, C. Keating, T. Mayer, *Nat. Nanotechnol.* **2008**, *3*, 88–92.
[16] V. Deshpande, H.-Y. Chiu, H. W. C. Postma, C. Miko, L. Forro, M. Bockrath, *Nano Lett.* **2006**, *6*, 1092–1095.

[17] T. Hertel, R. Walkup, P. Avouris, *Phys. Rev. B* **1998**, *58*, 13870–13873.
[18] R. Martel, T. Schmidt, H. Shea, T. Hertel, P. Avouris, *Appl. Phys. Lett.* **1998**, *73*, 2447–2449.
[19] W. Wei, Y. Liu, Y. Wei, K. Jiang, L.-M. Peng, S. Fan, *Nano Lett.* **2007**, *7*, 64–68.
[20] Z. Wang, R. Gao, W. de Heer, P. Poncharal, *Appl. Phys. Lett.* **2002**, *80*, 856–858.
[21] M. Doytscheva, M. Kaiser, N. de Jonge, *Nanotechnology* **2006**, *17*, 3226–3233.
[22] W. Jang, J. Lee, J.-B. Yoon, M.-S. Kim, J.-M. Lee, S.-M. Kim, K.-H. Cho, D.-W. Kim, D. Park, W.-S. Lee, *Appl. Phys. Lett.* **2008**, *92*, 103110.
[23] E. Pop, *Nano Res.* **2010**, *3*, 147–169.
[24] E. Pop, D. Mann, J. Cao, Q. Wang, K. Goodson, H. Dai, *Phys. Rev. Lett.* **2005**, *95*, 155505.
[25] ABAQUS/Explicit 6.4–1, User's Manual. **2003**.
[26] M. Dequesnes, Z. Tang, N. Aluru, *J. Eng. Mater. Technol.* **2004**, *126*, 230.
[27] L. Jonsson, S. Axelsson, T. Nord, S. Viefers, J. Kinaret, *Nanotechnology* **2004**, *15*, 1497–1502.
[28] B. Peng, M. Locascio, P. Zapol, S. Li, S. L. Mielke, G. C. Schatz, H. D. Espinosa, *Nat. Nanotechnol.* **2008**, *3*, 626–631.
[29] E. Minot, Y. Yaish, V. Sazonova, J.-Y. Park, M. Brink, P. McEuen, *Phys. Rev. Lett.* **2003**, *90*, 156401.
[30] J. Kinaret, T. Nord, S. Viefers, *Appl. Phys. Lett.* **2003**, *82*, 1287–1289.
[31] J. Jang, S. Cha, Y. Choi, G. Amaratunga, D. Kang, D. Hasko, J. Jung, J. Kim, *Appl. Phys. Lett.* **2005**, *87*, 263103.
[32] J. Jang, S. Cha, Y. Choi, D. Kang, T. Butler, D. Hasko, J. Jung, J. Kim, G. Amaratunga, *Nat. Nanotechnol.* **2008**, *3*, 26–30.
[33] J. Luo, Y. Fu, H. Le, J. Williams, S. Spearing, W. Milne, *J. Micromech. Microeng.* **2007**, *17*, S147–S163.
[34] S. Kwok, J. Wang, P. Chu, *Diamond Relat. Mater.* **2004**, *14*, 78–85.
[35] R. Needs, M. Mansfield, *J. Phys.: Condens. Matter* **1989**, *1*, 7555–7563.
[36] Y. Wang, T. Wang, X. Lin, V. Dravid, *Nanotechnology* **2006**, *17*, 6011–6015.
[37] M. Shiraishi, M. Ata, *Carbon* **2001**, *39*, 1913–1917.
[38] N. Kumar, H. Schmidt, M. Clark, A. Ross, B. Lin, L. Fredin, B. Baker, D. Patterson, W. Brookover, C. Xie, C. Hilbert, R. Fink, C. Potter, A. Krishnan, D. Eichman, *Soc. Inf. Display Dig.* **1994**, 43–46.
[39] P. A. Anderson, *Phys. Rev.* **1959**, *115*, 553.
[40] T. Tachibana, J. T. Glass, *Diamond Relat. Mater.* **1993**, *2*, 963–969.

Received: July 11, 2010
Revised: September 1, 2010
Published online: November 22, 2010